

Article

Manipulating Electrolyte Interface Chemistry Enables High-Performance TiO₂ Anode for Sodium-Ion Batteries

Qi Wang, Rui Zhang *, Dan Sun, Haiyan Wang * and Yougen Tang *

Hunan Provincial Key Laboratory of Chemical Power Sources, College of Chemistry and Chemical Engineering, Central South University, Changsha 410083, China; 202301039@csu.edu.cn (Q.W.); sundan4330@csu.edu.cn (D.S.)

* Correspondence: csuzr606@csu.edu.cn (R.Z.); wanghy419@csu.edu.cn (H.W.); ygtang@csu.edu.cn (Y.T.)

Abstract: Titanium dioxide (TiO₂) has emerged as a candidate anode material for sodium-ion batteries (SIBs). However, their applications still face challenges of poor rate performance and low initial coulomb efficiency (ICE), which are induced by the unstable solid-electrolyte interface (SEI) and sluggish Na⁺ diffusion kinetics in conventional ester-based electrolytes. Herein, inspired by the electrode/electrolyte interfacial chemistry, tetrahydrofuran (THF) is exploited to construct an advanced electrolyte and reveal the relationship between the improved electrochemical performance and the derived SEI film on TiO₂ anode. The robust and homogeneously distributed F-rich SEI film formed in THF electrolyte favors fast interfacial charge transfer dynamics and excellent interfacial stability. As a result, the THF electrolyte endows the TiO₂ anode with greatly improved ICE (64.5%), exceptional rate capabilities (186 mAh g⁻¹ at 5.0 A g⁻¹), and remarkable cycling stability. This study elucidates the control of interfacial chemistry by rational electrolyte design and offers insights into the development of high-performance and long-lifetime TiO₂ anode.

Keywords: sodium-ion batteries; titanium dioxide; electrolyte modulation; interfacial chemistry; solid electrolyte interface



Citation: Wang, Q.; Zhang, R.; Sun, D.; Wang, H.; Tang, Y. Manipulating Electrolyte Interface Chemistry Enables High-Performance TiO₂ Anode for Sodium-Ion Batteries. *Batteries* **2024**, *10*, 362. <https://doi.org/10.3390/batteries10100362>

Academic Editor: Claudio Gerbaldi

Received: 11 September 2024

Revised: 1 October 2024

Accepted: 9 October 2024

Published: 11 October 2024



Copyright: © 2024 by the authors. Licensee MDPI, Basel, Switzerland. This article is an open access article distributed under the terms and conditions of the Creative Commons Attribution (CC BY) license (<https://creativecommons.org/licenses/by/4.0/>).

1. Introduction

Sodium-ion batteries (SIBs) are proposed as a viable candidate for lithium-ion batteries (LIBs), stemming from the cost-effective and widespread availability of sodium resources [1,2]. Among numerous anode materials, titanium dioxide (TiO₂) has been regarded as a promising anode candidate in SIBs, considering its high theoretical capacity (335 mAh g⁻¹), natural abundance, and low cost [3,4]. Unfortunately, the low inherent electronic conductivity and slow Na⁺ diffusion kinetics substantially deteriorate the rate performance of TiO₂ anodes [5]. To address this issue, extensive strategies, including sophisticated nanostructure design [6], hybridization with carbonaceous materials [7], creation of crystal defects [8], and heteroatom doping [9], have been proposed to accelerate ion/electron transportation in the bulk phase of TiO₂. Nevertheless, the modulation of the electrode/electrolyte interface is also an effective method to promote the reaction kinetics of the TiO₂ electrode.

The electrolyte, as the “blood” of the battery, not only conducts Na⁺ but also directly determines the interfacial properties [10,11]. Specifically, it significantly affects the desolvation kinetics and ion transport through the solid electrolyte interphase (SEI) [12,13]. Currently, commonly used carbonate esters, such as ethylene carbonate (EC), propylene carbonate (PC), etc., have strong interactions with cations, resulting in slow Na⁺ desolvation [14]. In addition, the generated unstable SEI hinders interfacial ion transport, leading to continuous electrolyte depletion, thus causing poor cycling stability and rate performance [15]. Compared to the esters, ether solvents have much lower interactions with cations, demonstrating significantly accelerated desolvation kinetics, in addition, the higher lowest unoccupied molecular orbital (LUMO) of ether solvent/cations compounds,

leading to better reduction stability [16]. Therefore, ether electrolytes are widely appreciated in metal alloys [17], carbonaceous materials [18], TiO_2 anodes [19], etc. [20], which can significantly improve electrochemical performance [21]. Tetrahydrofuran (THF), as a cyclic ether, has a weaker solvation ability than some linear ether molecules (such as 1,2-dimethoxyethane) [22]. Although the THF-based electrolytes have been investigated in other electrode materials and exhibited improved electrochemical properties, to our knowledge, the compatibility of THF electrolytes with TiO_2 and its effect on SEI formation have not been systematically studied [23].

Herein, we systematically investigate the effect of THF electrolytes on the sodium storage properties of TiO_2 anode materials and the derived SEI film. Temperature-dependent EIS and kinetic analyses revealed that the charge transfer energy barrier in THF electrolytes is significantly lower than that in EC/DEC electrolytes, contributing to the greatly accelerated Na^+ transfer kinetics. Moreover, the chemical composition and structural morphology of the SEI film are analyzed. The results show that the THF electrolyte can induce the formation of homogeneous and stable SEI film on the TiO_2 anode surface, effectively enhancing interfacial stability and reducing electrolyte decomposition. Consequently, the TiO_2 anode with THF electrolytes achieves a greatly improved ICE of 64.5% and remarkable cycling stability. This strategy for modulating SEI chemistry is expected to provide essential guidance for the development of other high-performance anodes.

2. Materials and Methods

2.1. Materials

Ethylene carbonate (EC), diethyl carbonate (DEC), tetrahydrofuran (THF), and sodium hexafluorophosphate (NaPF_6) were purchased from DoDoChem. Commercial anatase TiO_2 was obtained from Macklin Inc. (Rochelle, IL, USA) and used without additional purification.

2.2. Materials Characterization

X-ray diffraction (XRD, Cu $\text{K}\alpha$ radiation, Nickel plate, Rigaku Ultima IV, Tokyo, Japan) was used to identify the phase structure of commercial anatase. Scanning electron microscopy (SEM, JEOL/JSM-7610FPlus, Tokyo, Japan) examined the surface morphologies with an applied voltage of 10 kV. Transmission electron microscopy (TEM, JEOL/JEM-F200, Tokyo, Japan) obtained the images of the different SEI structures using an applied voltage of 200 kV. The chemical compositions of SEI on the TiO_2 surface were characterized by X-ray photoelectron spectroscopy measurements (XPS, Thermo Fisher Scientific, Waltham, MA, USA; the detailed test steps are included in the Supplementary Information). Before TEM and XPS characterizations, the cycled TiO_2 anodes were washed with DEC or THF and dried in a vacuum.

2.3. Electrochemical Measurements

The electrochemical performance was evaluated by assembling CR2016-type coin cells in an Ar-filled glove box (both H_2O and O_2 content < 0.1 ppm). For TiO_2 electrodes, it was fabricated by uniformly coating the slurry composed of 70 wt% TiO_2 , 20 wt% Super P, and 10 wt% polyvinylidene fluoride (PVDF) on copper foil, which was dried in a vacuum at 80 °C overnight. The active material loading was 1.0~1.5 mg cm⁻². The Na metal was used as the counter/reference electrode, and the glass fiber was applied as the separator. 1.0 M NaPF_6 in THF or a mixture of EC and DEC ($v/v = 1:1$) was adopted as the electrolyte. The galvanostatic discharge/charge tests were performed on Neware CT-3008W with a cutoff voltage of 0.01 to 3 V. Cyclic voltammetry (CV) and electrochemical impedance spectra (EIS) were collected on a CHI760E electrochemical workstation (chenhua, Shanghai, China).

3. Results

The morphology and phase structure of commercial TiO_2 were characterized by SEM, TEM, and XRD. Figure 1 shows that commercial TiO_2 powder is composed of particles with

a particle size of tens of nanometers, and all diffraction peaks can be indexed to anatase TiO_2 (JCPDS 21-1272) [24].

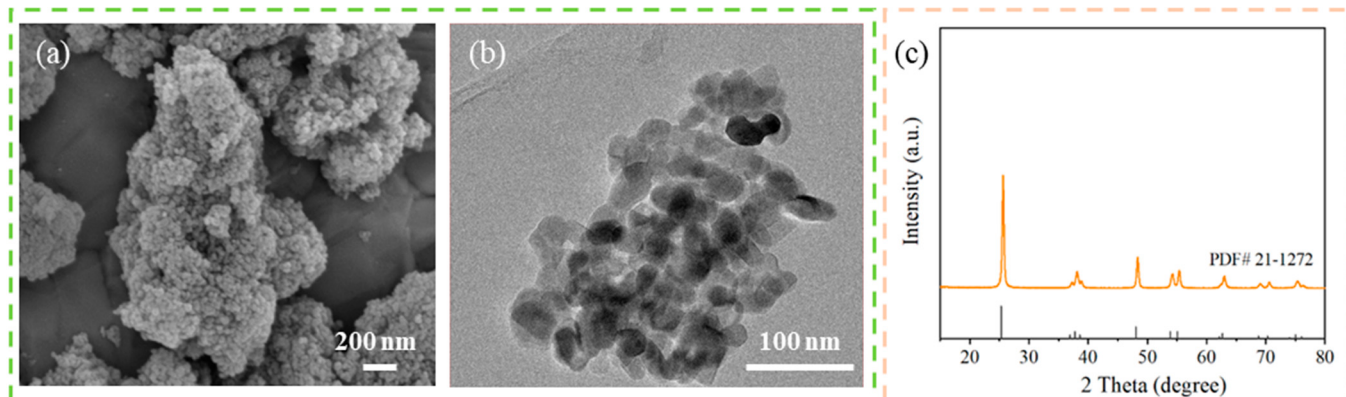


Figure 1. Morphological and phase structure characterization of the commercial TiO_2 . (a) SEM and (b) TEM images, (c) XRD pattern.

Half cells were fabricated to compare the electrochemical behaviors of TiO_2 electrodes in EC/DEC- and THF-based electrolytes. As shown in Figure 2a, two reduction peaks located at 0.78 and 0.44 V in the EC/DEC electrolyte during the first discharge, which disappears in subsequent sweeps, correspond to the SEI formation, and the peak at 0.01–0.3 V is associated with irreversible amorphization upon the initial sodiation process, reflecting that the anatase phase is transformed into the amorphous sodium titanate phase [25]. Sharply contrast, the CV curves in THF electrolytes exhibit quite different features. The irreversible broad reduction peaks indexed to the SEI formation are weaker, showing less THF electrolyte decomposition. In addition, the well-shaped redox pair peaks around 0.8 V are ascribed to Na^+ insertion/extraction, and the higher overlap degree can be observed in the following scan cycles, demonstrating better electrochemical reversibility [3]. Electrolyte decomposition can be inhibited due to the better reduction stability of the THF electrolyte. Thus, the THF electrolyte displays higher initial charge capacity and Coulombic efficiency. These conclusions are further verified by galvanostatic charge/discharge results.

Figure 2b displays the initial charge/discharge curves. As seen, the charge/discharge capacity of THF electrolyte is $278/431 \text{ mAh g}^{-1}$, corresponding to an ICE of 64.5%, whereas the charging/discharging capacity of EC/DEC electrolyte is $249/621 \text{ mAh g}^{-1}$ with a much lower ICE of 40.1%. Numerous studies have shown that ether solvents (such as DME, THF, etc.) have a higher LUMO energy level compared to ester solvents and are more difficult to reduce, resulting in less electrolyte decomposition, which is conducive to improving ICE [26]. It can be seen that the first discharge capacity of EC/DEC and THF electrolytes both exceeds the theoretical specific capacity of 335 mAh/g since electrolyte decomposition and side reactions occur during the initial discharge process. The rate performances of two electrolytes are investigated as shown in Figure 2c–e, the specific capacities of THF electrolytes are $285, 246, 227, 215, 206$, and 197 mAh g^{-1} at $0.05, 0.1, 0.2, 0.5, 1$, and 2 A g^{-1} , respectively. Even if the current is up to 5 A g^{-1} , the THF electrolyte maintains a capacity of 186 mAh g^{-1} , while the capacity of the EC/DEC electrolyte is only 51 mAh g^{-1} . Notably, both EC/DEC and THF electrolytes show significant capacity attenuation at 50 mA g^{-1} , possibly due to the continued evolution of the SEI film during the first few cycles. In addition, the THF electrolyte exhibits better cycling stability in contrast with the EC/DEC electrolyte. In Figure 2f, the THF electrolyte still delivers a high specific capacity of 168 mAh g^{-1} with an almost 100% capacity retention after 1000 cycles at 2 A g^{-1} , while the capacity of EC/DEC electrolyte decays rapidly. Particularly, at an ultra-high current of 5 A g^{-1} , the reversible capacity of the THF electrolyte maintains 150 mAh g^{-1} with a capacity retention of 78.5% after 2400 cycles (Figure 2g,h). The results show that the THF electrolyte significantly enhances the comprehensive electrochemical

performance of the TiO_2 anode, which is superior to some reported advanced TiO_2 anodes based on ether electrolytes [5,9,19,27,28].

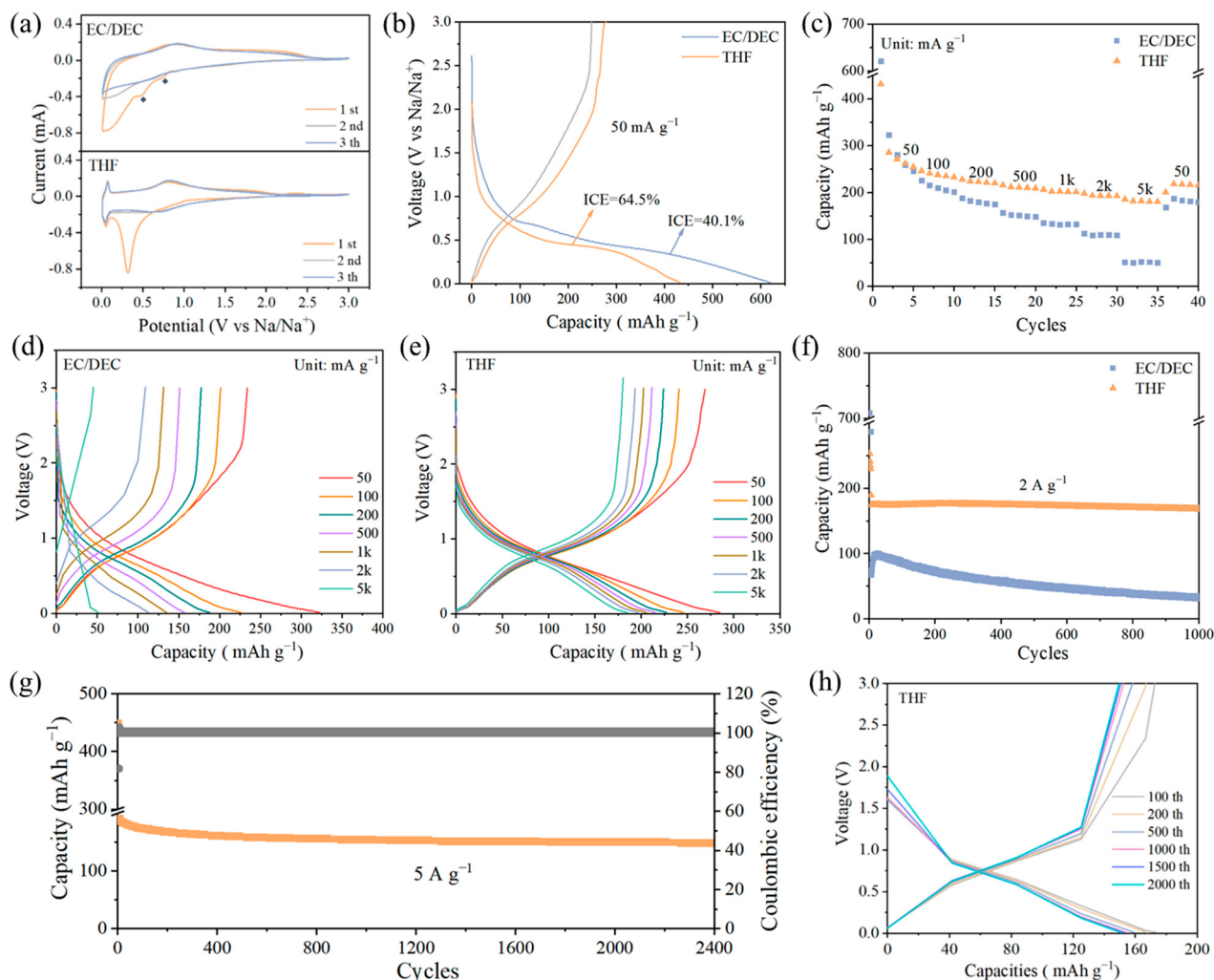


Figure 2. Electrochemical performance of TiO_2 anode using different electrolytes. (a) CV curves at 0.2 mV s^{-1} . (b) Initial charge/discharge profiles at 50 mA g^{-1} . (c) Rate performance. The charge/discharge profiles of TiO_2 electrodes at various current densities in (d) EC/DEC and (e) THF electrolytes. (f) Cycling performance of EC/DEC and THF-based electrolytes at 2 A g^{-1} . (g) Long-term cycling performance and (h) the corresponding charge/discharge profiles of THF electrolyte at 5 A g^{-1} .

Transport behavior and kinetic performance of Na^+ across the TiO_2 electrode in THF and EC/DEC were first investigated by CV tests. The CV curves in THF electrolyte at different scan rates show similar shapes, indicating mild polarization and better redox reversibility, whereas, in EC/DEC, the CV curves begin to deform and more severe polarization as the scan rate increases (Figure 3a,b) [29]. The Na^+ storage mechanism of the electrode can be further investigated according to the relationship between the peak currents and sweep rates [30]. Based on the following equation [31]:

$$i = av^b \quad (1)$$

the calculated b -values for EC/DEC and THF electrolytes are 0.816 and 0.919, respectively (Figure 3c), indicating that the charge in the THF electrolyte is more controlled by the

pseudocapacitive behavior [32]. Figure 3d,e shows the pseudocapacitive contributions of both electrolytes at 1.0 mV s^{-1} . According to the following equation [33]:

$$i = k_1 v + k_2 v^{1/2} \quad (2)$$

as anticipated, the pseudocapacitive contribution of THF is quantified as 70.4% to whole charge storage, surpassing 30% compared to the EC/DEC electrode (39.4%). Furthermore, the pseudocapacitance contribution of THF electrolyte is higher than that of EC/DEC electrolyte at different scanning rates, which further indicates the higher pseudocapacitance behavior of THF electrolyte (Figure 3f,g). Na^+ diffusion coefficients (D_{Na^+}) were also measured using the galvanostatic intermittent titration technique (GITT) tests [20]. As depicted in Figure 3h,i, it is clear that the THF electrolyte has significantly higher D_{Na^+} values at all potentials compared to the EC/DEC electrolyte, suggesting an enhanced sodium storage kinetic of the THF electrolyte, which fits well with the superior rate capability. Both the elevated pseudocapacitive contribution and higher D_{Na^+} verify the promoted Na^+ reaction kinetics, resulting in outstanding rate capability and high capacity of TiO_2 electrodes in THF electrolyte [2].

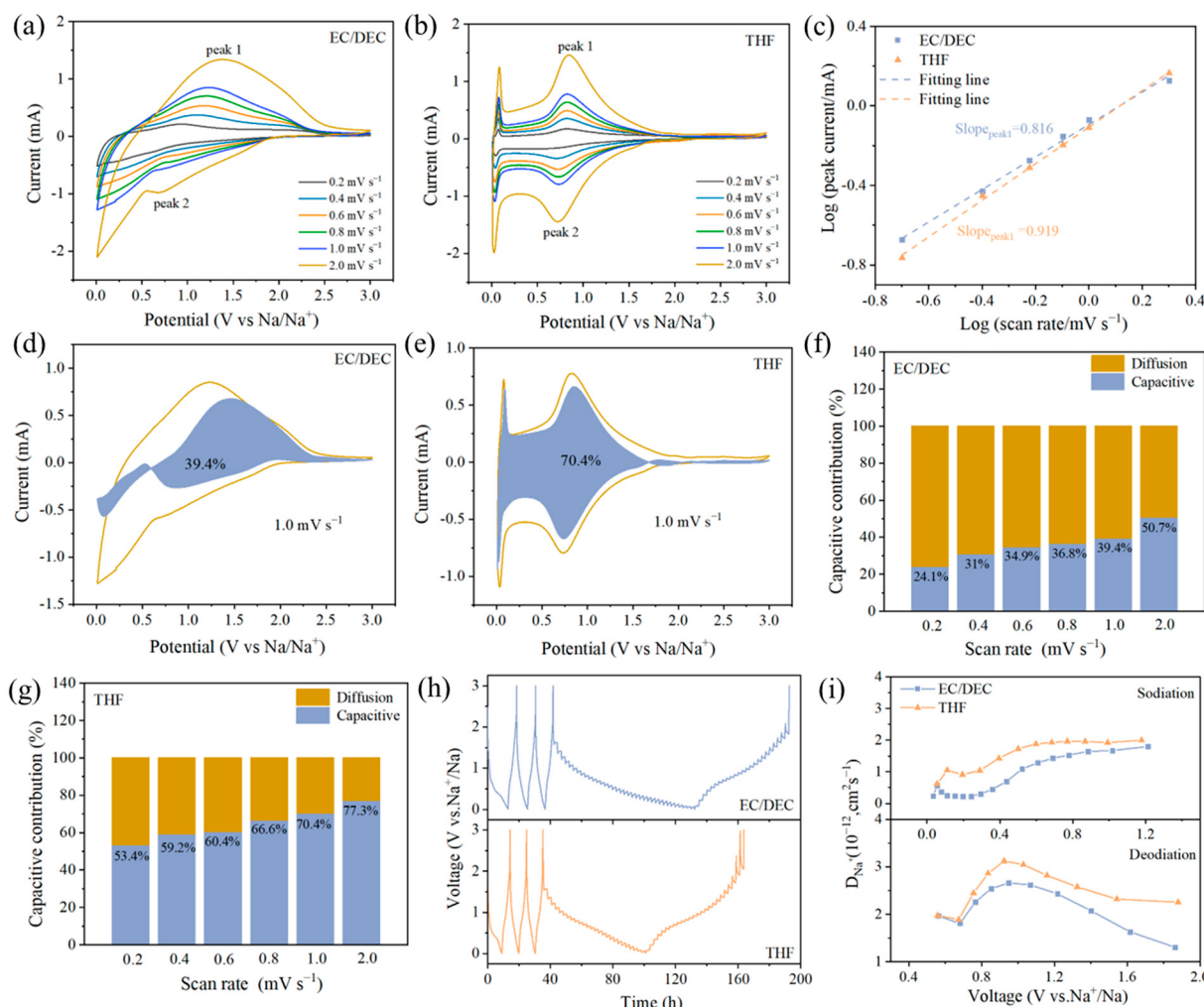


Figure 3. CV curves of (a) EC/DEC and (b) THF electrolytes at various scanning rates, (c) b-value of the two electrolytes. (d,e) Capacitance contributions at 1 mV s^{-1} . (f,g) Capacitance contribution at various scanning rates. (h) GITT curves with EC/DEC and THF electrolytes, (i) the calculated Na^+ diffusion coefficients.

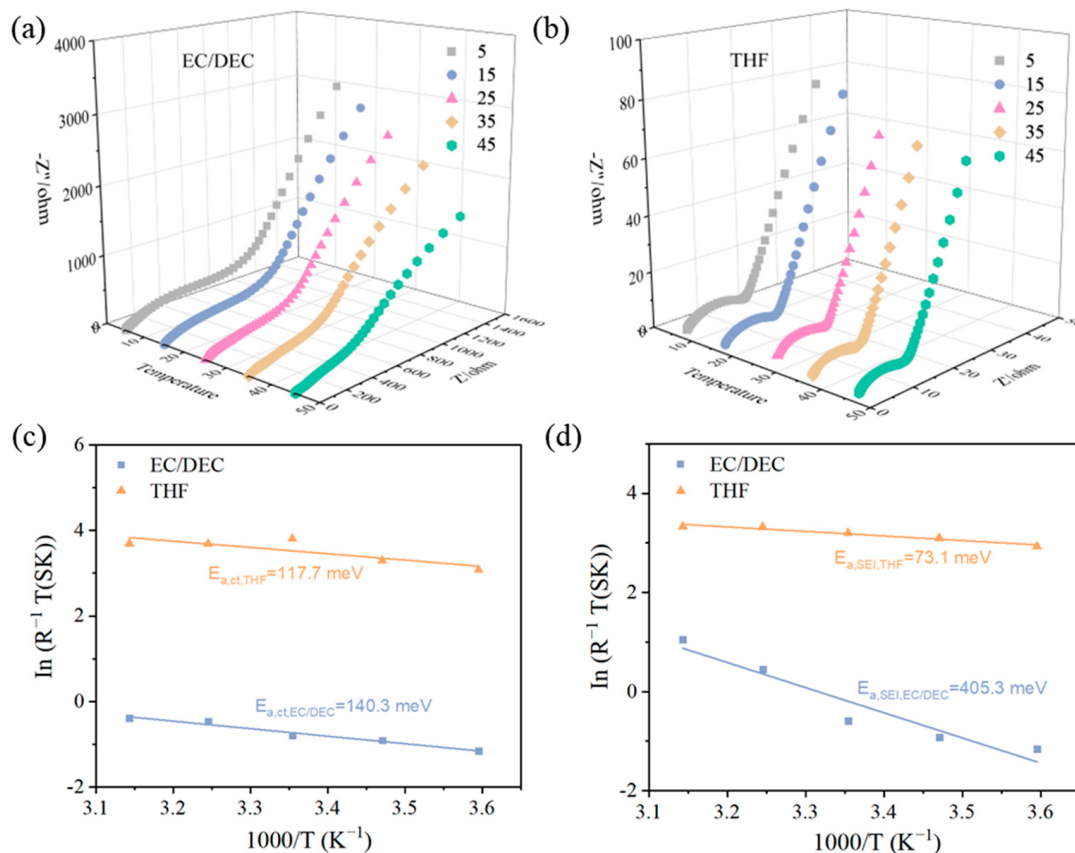


Figure 4. Nyquist plots at different temperatures in (a) EC/DEC and (b) THF electrolytes. Corresponding activation energies (c) $E_{a,ct}$ and (d) $E_{a,SEI}$ derived by Arrhenius fitting.

To acquire a deeper understanding of the faster dynamics, the temperature-dependent EIS was also analyzed from 5 °C to 45 °C (Figure 4a,b). The impedance in the EC/DEC decreases sharply with increasing temperature; in stark contrast, that in the THF electrolyte is consistently lower and more stable throughout the temperature range. The corresponding activation energies are calculated according to the classical Arrhenius equation [34]:

$$\sigma T = A \exp(-E_a/k_B T) \quad (3)$$

R_{SEI} and R_{ct} are obtained by fitting with an equivalent circuit (Figure S1). As shown in Figure 4c,d, the THF electrolyte exhibits a smaller E_{ct} value of 117.7 meV than that in EC/DEC (140.3 meV), offering accelerated charge transfer across the electrode/electrolyte interface [35]. Notably, in EC/DEC electrolyte, the $E_{a,SEI}$ is 5.5 times (405.3 meV) higher than that in THF electrolyte, suggesting that there is a large difference between EC/DEC and THF electrolyte-derived SEI films, and the Na^+ can transfer more rapidly across the SEI in THF electrolyte, which collectively achieves the rapid electrochemical reaction kinetics [36].

The interfacial resistance of EC/DEC and THF electrolytes after different cycles was also compared in Figure 5. The results show that the R_{SEI} and R_{ct} of EC/DEC electrolytes are consistently higher than THF electrolytes as the cycle progresses (Figure 5a,b and Table S1). Specifically, the R_{ct} of EC/DEC electrolytes (1059Ω) was several hundred times higher than in THF electrolytes (5.58Ω) after 50 cycles, indicating higher interfacial diffusion resistance and slow charge transfer kinetics (Figure 5c) [37]. In contrast, the cells with THF electrolyte present marginally increased resistances and better electrode/electrolyte interface stability during subsequent cycles, thus contributing to superior cycling stability.

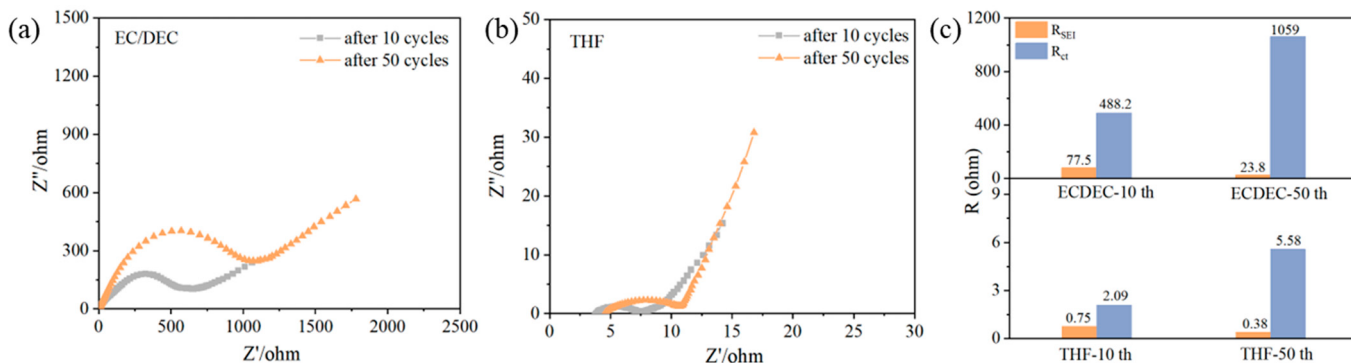


Figure 5. Nyquist plots after different cycles of (a) EC/DEC and (b) THF electrolytes. (c) The corresponding values of R_{SEI} and R_{ct} .

In general, the superior rate capability and higher ICE of THF electrolytes compared to EC/DEC electrolytes should be closely related to better interfacial properties [13]. Therefore, HRTEM was first employed to characterize the microstructures of SEI. An extremely thin SEI layer with a thickness of 1.2 nm is covered on the TiO_2 anode in THF, whereas an uneven and relatively thick SEI (7.3 nm) is observed in the EC/DEC electrolyte (Figure 6a,b). The results indicate that THF can generate a stable and robust SEI during cycling, which is consistent with a low and stable R_{SEI} value, thus effectively reducing electrolyte decomposition and stabilizing the interface [38].

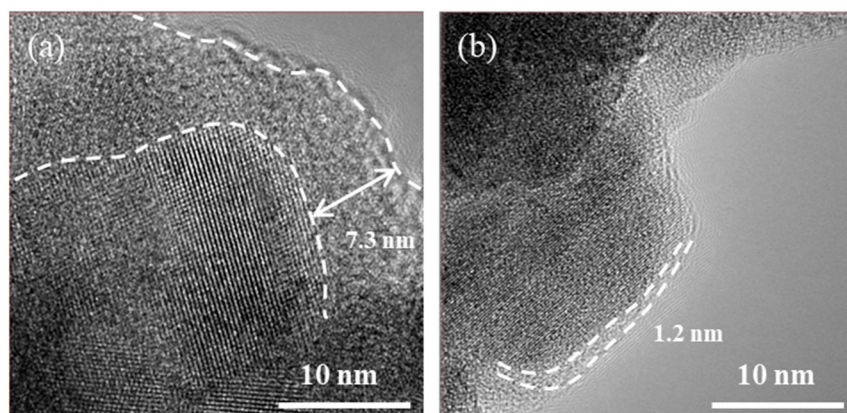


Figure 6. HRTEM images of TiO_2 anode after three cycles in (a) EC/DEC and (b) THF electrolytes.

The chemical composition of the SEI in both electrolytes after cycling was further examined using XPS characterizations. Figures 7 and S2 show the high-resolution C 1s, F 1s, Na 1s, Ti 2p, and O 1s XPS spectra, and the composition differences of SEI films of the two electrolytes can be obtained by combining the changes of these spectra (Tables S2 and S3). In the EC/DEC electrolyte, large amounts of C–O (286.5 eV), C=O (288.3 eV), and CO_3^{2-} (289.9 eV) are observed in the C 1s spectra due to electrolyte decomposition to produce $ROCO_2Na$ and Na_2CO_3 , which is further verified by O 1s spectra (Figure S2a,d) [39]. It is worth noting that the intensity of the Ti–O bond in THF is much higher than that of EC/DEC, and it can be inferred that more TiO_2 is exposed in THF and less SEI film composition is generated, which is consistent with the results observed in the Ti 2p spectrum (Figure S2c,f). In the F 1s spectra, Na-F (683.8 eV) and C-F (687.1 eV) are derived from $NaPF_6$ decomposition and PVDF, respectively (Figure 7b,e). Combined with the above analysis, it can be concluded that SEI film in EC/DEC electrolytes contains more organic phases ($ROCO_2Na$) and inorganic materials (Na_2CO_3), while in THF, the content of inorganic NaF is higher, indicating that the electrolyte decomposition can effectively promote the construction of an F-rich interface. Note that the inorganic-rich SEI generally exhibits low interfacial impedance, fast Na^+ diffusion kinetics, and excellent electrochemical stabil-

ity [18]. As the sputtering depth increases (Figure 7c,f), it can be observed that the C and O contents decrease and the Na content increases in the EC/DEC electrolyte, presenting an inhomogeneous combination of inorganic and organic species. In contrast, the contents of various elements in the THF electrolyte do not change much, and the evenly distributed SEI ensures rapid Na^+ diffusion and interfacial stabilization [40].

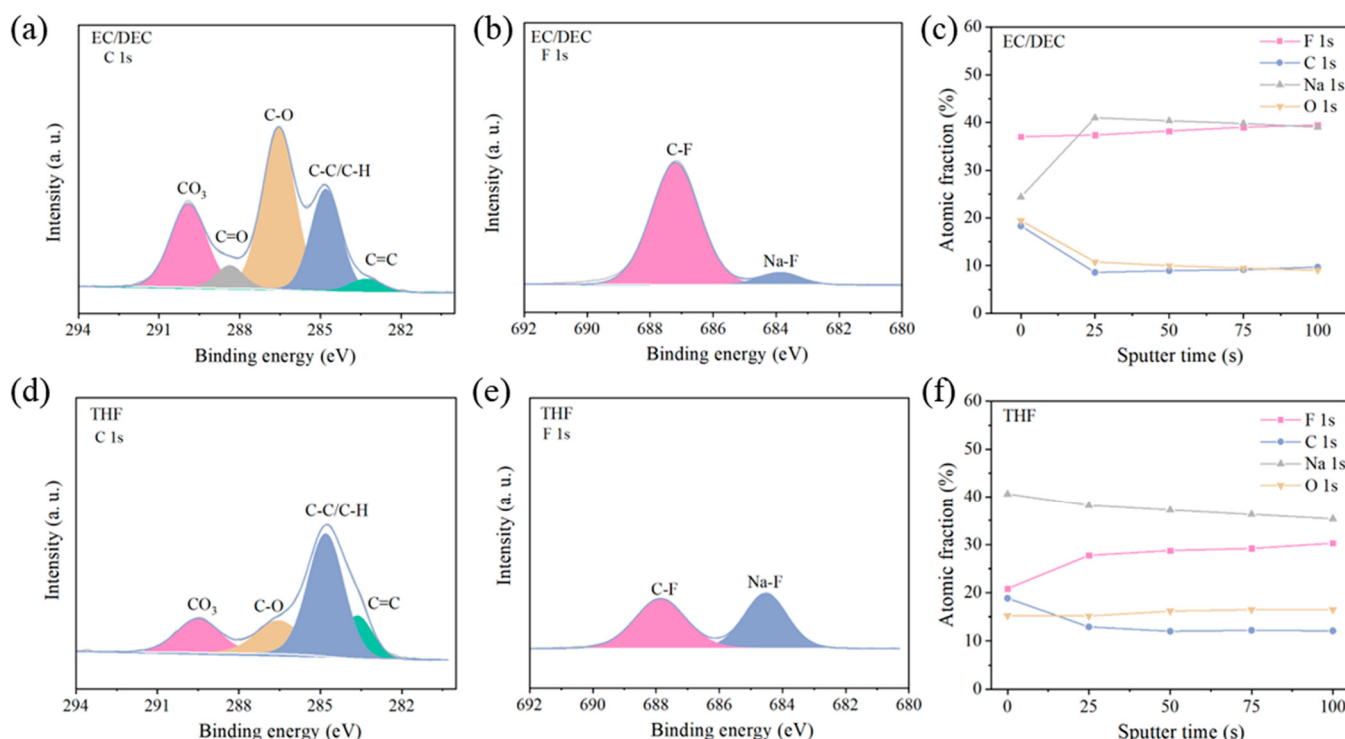


Figure 7. XPS characterization of the SEI. (a) C 1s (b) F 1s spectra and (c) elemental sputter-depth profile of TiO_2 anodes cycled in EC/DEC electrolyte. (d) C 1s (e) F 1s spectra and (f) elemental sputter-depth profile of TiO_2 anodes cycled in THF electrolyte.

The superiority of THF-derived SEI film was further validated through SEM. Compared with the pristine TiO_2 electrode (Figure 8a,d), some flower-like particles are formed on the surface of the TiO_2 anode in EC/DEC after 100 cycles (Figure 8b), and after further cycling up to 500 cycles, these flower-like particles completely cover the electrode surface (Figure 8c), leading to the elimination of original porous structure of the electrode. According to the previous literature, these needle-like compounds may be some sodium oxygen inorganic substances produced by the decomposition of electrolytes [41,42]. In THF electrolyte, the overall porous shape of the TiO_2 electrode remains intact and the particles are clear after 500 cycles (Figure 8e,f). The SEM results can further verify the instability of SEI generated in EC/DEC electrolytes, and thus, continuous electrolyte decomposition leads to SEI growth, increased impedance, and electrochemical performance degradation. By contrast, the SEI induced in THF electrolyte is more stable and the electrode surface does not change significantly during long-term cycling.

Typically, in conventional carbonate-based electrolytes, the intimate Na^+ -solvent affinity causes sluggish Na^+ desolvation at interphase, contributing to the increased polarization [43]. Furthermore, EC and DEC are prone to decompose and reduce to form fragile organic-rich SEI during electrochemical cycling, which is easily dissolved in the electrolyte, leading to continuous electrolyte decomposition, further exacerbating the generation of side-reactions and rapid capacity decay [44], as shown in Figure 9a. Conversely, in the THF electrolyte (Figure 9b), the charge transfer energy barrier at the interface is lower, which facilitates the interphase charge transfer process. In addition, the generated stable and conformal SEI can lead to fast and uniform ion diffusion and stable cycling performance.

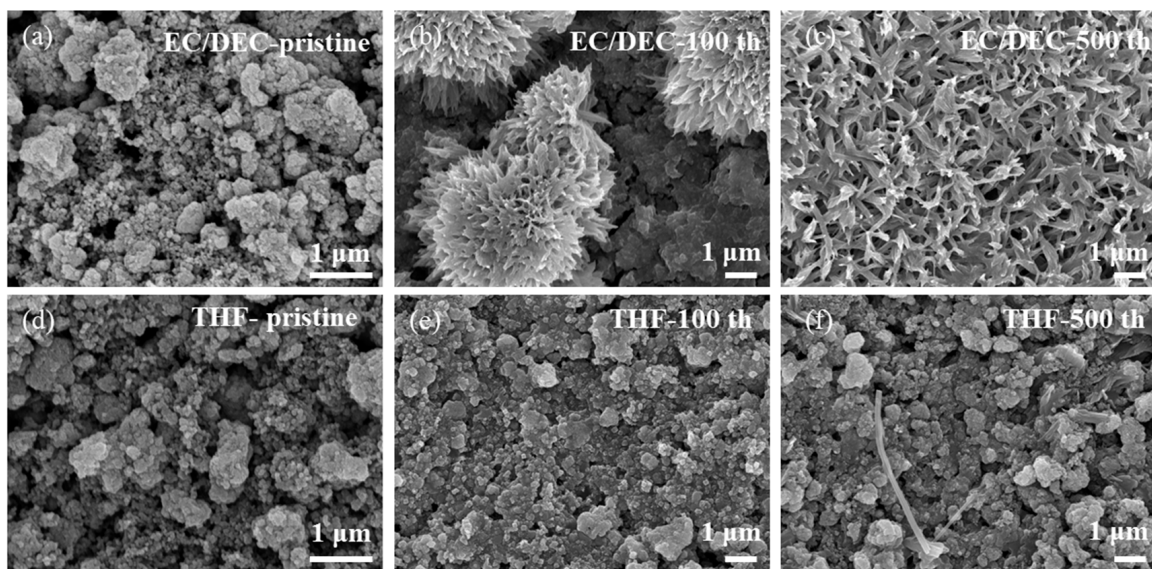


Figure 8. SEM images of TiO_2 anodes before and after cycling at 1 A g^{-1} . (a–c) TiO_2 anode with EC/DEC electrolyte. (d–f) TiO_2 anode with THF electrolyte.

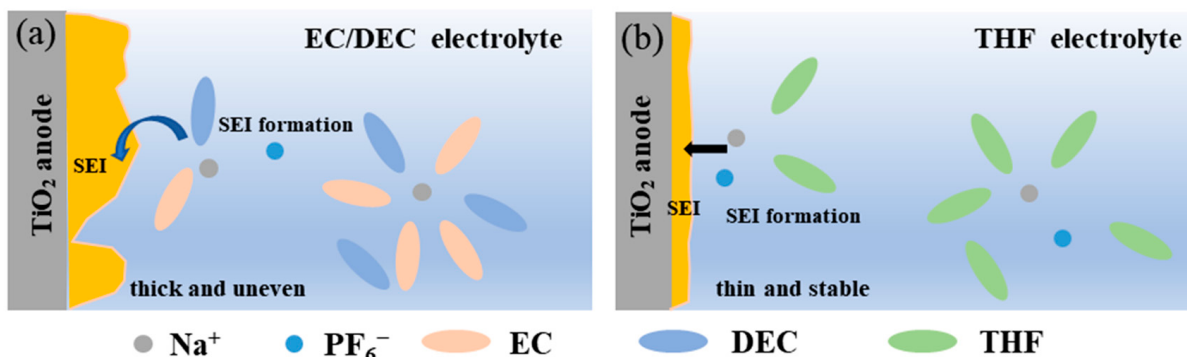


Figure 9. Schematic illustrations of the electrolyte structure and SEI formation process on TiO_2 anodes (a) in EC/DEC electrolyte and (b) THF electrolyte.

4. Conclusions

In this work, a cyclic ether, THF, was introduced to regulate electrode/electrolyte interphase. The electrochemical data coupled with detailed electrode postmortem analysis showed that a homogeneous and stable SEI film was successfully constructed on the TiO_2 anode by the THF electrolyte. The induced SEI films not only accelerated Na^+ diffusion and charge transfer kinetics but also enhanced electrode/electrolyte interface stability during repeated cycling. Benefiting from these advantages, the TiO_2 anode exhibited exceptional performance with an outstanding rate performance (186 mAh g^{-1} at 5 A g^{-1}) and superior cycling stability (94.6% capacity retention after 1000 cycles), which outperforms other reported ether electrolytes. This work provides informative insights into electrolyte chemistry and interfacial modulation and guides the development of high-performance TiO_2 anode for SIBs.

Supplementary Materials: The following supporting information can be downloaded at: <https://www.mdpi.com/article/10.3390/batteries10100362/s1>, Figure S1: The equivalent circuit for the EIS fitting. Figure S2: XPS characterization of SEI in (a–c) EC/DEC and (d–f) THF electrolytes. Table S1: Impedance parameters of EC/DEC and THF electrolytes at different cycles. Table S2: XPS binding energy and peak assignment for the SEI components formed in EC/DEC electrolyte. Table S3: XPS binding energy and peak assignment for the SEI components formed in THF electrolyte.

Author Contributions: Q.W. wrote the original draft. R.Z. reviewed and edited. D.S., Y.T. and H.W. supervised and provided funding acquisition. All authors have read and agreed to the published version of the manuscript.

Funding: The work was supported by the National Nature Science Foundation of China (21975289), the Science and Technology Innovation Program of Hunan Province (2022RC3050), the Hunan Provincial Science and Technology Plan Project of China (2017TP1001), the Postdoctoral Fellowship Program of CPSF (GZC20233152) and the China Postdoctoral Science Foundation Funded Project (2024M753673).

Data Availability Statement: The data presented in this study are available on request from the corresponding author.

Conflicts of Interest: The authors declare no conflicts of interest.

References

- Chen, L.; Chen, M.; Meng, Q.; Zhang, J.; Feng, G.; Ai, X.; Cao, Y.; Chen, Z. Reconstructing Helmholtz Plane Enables Robust F-Rich Interface for Long-Life and High-Safe Sodium-Ion Batteries. *Angew. Chem. Int. Ed.* **2024**, *63*, e202407717. [[CrossRef](#)]
- Zhong, L.; Yue, M.; Liang, Y.; Xi, B.; An, X.; Xiao, Y.; Cheng, B.; Lei, S.; Xiong, S. In Situ Universal Construction of Thiophosphate/MXene Hybrids via Lewis Acidic Etching for Superior Sodium Storage. *Adv. Funct. Mater.* **2024**, *24*, 07740. [[CrossRef](#)]
- Wang, Q.; Tang, Z.; Zhang, R.; Sun, D.; Fu, L.; Tang, Y.; Li, H.; Xie, H.; Wang, H. Significantly Improving the Initial Coulombic Efficiency of TiO₂ Anode for Sodium-Ion Batteries. *ACS Appl. Mater. Interfaces* **2023**, *15*, 40508–40518. [[CrossRef](#)] [[PubMed](#)]
- Hao, Z.; Lyu, J.; Tian, M.; Zhang, X.; Wang, K.; Yang, S.-W.; Zhang, Y.; Xu, G.Q. Unraveling the Synergistic Effects of Oxygen Vacancy and Amorphous Structure on TiO₂ for High-Performance Lithium Storage. *Small Struct.* **2024**, *5*, 2300442. [[CrossRef](#)]
- Lv, D.; Wang, D.; Wang, N.; Liu, H.; Zhang, S.; Zhu, Y.; Song, K.; Yang, J.; Qian, Y. Nitrogen and fluorine co-doped TiO₂/carbon microspheres for advanced anodes in sodium-ion batteries: High volumetric capacity, superior power density and large areal capacity. *J. Energy Chem.* **2022**, *68*, 104–112. [[CrossRef](#)]
- He, H.; Gan, Q.; Wang, H.; Xu, G.-L.; Zhang, X.; Huang, D.; Fu, F.; Tang, Y.; Amine, K.; Shao, M. Structure-dependent performance of TiO₂/C as anode material for Na-ion batteries. *Nano Energy* **2018**, *44*, 217–227. [[CrossRef](#)]
- Diao, Z.; Wang, Y.; Zhao, D.; Zhang, X.; Mao, S.S.; Shen, S. Ultra-small TiO₂ nanoparticles embedded in carbon nanosheets for high-performance sodium storage. *Chem. Eng. J.* **2021**, *417*, 127928. [[CrossRef](#)]
- Gan, Q.; He, H.; Zhu, Y.; Wang, Z.; Qin, N.; Gu, S.; Li, Z.; Luo, W.; Lu, Z. Defect-Assisted Selective Surface Phosphorus Doping to Enhance Rate Capability of Titanium Dioxide for Sodium Ion Batteries. *ACS Nano* **2019**, *13*, 9247–9258. [[CrossRef](#)]
- Fan, M.; Lin, Z.; Zhang, P.; Ma, X.; Wu, K.; Liu, M.; Xiong, X. Synergistic Effect of Nitrogen and Sulfur Dual-Doping Endows TiO₂ with Exceptional Sodium Storage Performance. *Adv. Energy Mater.* **2021**, *11*, 2003037. [[CrossRef](#)]
- Zheng, J.; Hu, C.; Nie, L.; Zang, S.; Chen, H.; Chen, N.; Ma, M.; Lai, Q. Electrolyte manipulation enhanced pseudo-capacitive K-storage for TiO₂ anode. *Appl. Surf. Sci.* **2023**, *611*, 155617. [[CrossRef](#)]
- Tan, L.; Huang, X.; Yin, T.; Guo, Y.; Ning, T.; Mei, Y.; Zou, K.; Li, L.; Ji, X.; Zou, G. A 5 V ultrahigh energy density lithium metal capacitor enabled by the fluorinated electrolyte. *Energy Storage Mater.* **2024**, *71*, 103692. [[CrossRef](#)]
- Zhang, Y.-Y.; Zhang, C.-H.; Guo, Y.-J.; Fan, M.; Zhao, Y.; Guo, H.; Wang, W.-P.; Tan, S.-J.; Yin, Y.-X.; Wang, F.; et al. Refined Electrolyte and Interfacial Chemistry toward Realization of High-Energy Anode-Free Rechargeable Sodium Batteries. *J. Am. Chem. Soc.* **2023**, *145*, 25643–25652. [[CrossRef](#)]
- Tang, X.; Xie, F.; Lu, Y.; Mao, H.; Chen, Z.; Pan, H.; Weng, S.; Yang, Y.; Li, X.; Guo, Z.; et al. Kinetics Manipulation for Improved Solid Electrolyte Interphase and Reversible Na Storage. *ACS Energy Lett.* **2024**, *9*, 1158–1167. [[CrossRef](#)]
- Yao, Q.; Zheng, C.; Ji, D.L.; Du, Y.Z.; Su, J.; Wang, N.A.; Yang, J.; Dou, S.X.; Qian, Y.T. Superior sodophilicity and molecule crowding of crown ether boost the electrochemical performance of all-climate sodium-ion batteries. *Proc. Natl. Acad. Sci. USA* **2024**, *121*, e2312337121. [[CrossRef](#)] [[PubMed](#)]
- Peng, X.; Liu, B.; Chen, J.; Jian, Q.; Li, Y.; Zhao, T. A Steric-Hindrance-Induced Weakly Solvating Electrolyte Boosting the Cycling Performance of a Micrometer-Sized Silicon Anode. *ACS Energy Lett.* **2023**, *8*, 3586–3594. [[CrossRef](#)]
- Jin, Y.; Le, P.M.L.; Gao, P.; Xu, Y.; Xiao, B.; Engelhard, M.H.; Cao, X.; Vo, T.D.; Hu, J.; Zhong, L.; et al. Low-solvation electrolytes for high-voltage sodium-ion batteries. *Nat. Energy* **2022**, *7*, 718–725. [[CrossRef](#)]
- Wang, C.; Wang, L.; Li, F.; Cheng, F.; Chen, J. Bulk Bismuth as a High-Capacity and Ultralong Cycle-Life Anode for Sodium-Ion Batteries by Coupling with Glyme-Based Electrolytes. *Adv. Mater.* **2017**, *29*, 1702212. [[CrossRef](#)]
- Tang, Z.; Wang, H.; Wu, P.-F.; Zhou, S.-Y.; Huang, Y.-C.; Zhang, R.; Sun, D.; Tang, Y.-G.; Wang, H.-Y. Electrode–Electrolyte Interfacial Chemistry Modulation for Ultra-High Rate Sodium-Ion Batteries. *Angew. Chem. Int. Ed.* **2022**, *61*, e202200475. [[CrossRef](#)]
- Xu, Z.-L.; Lim, K.; Park, K.-Y.; Yoon, G.; Seong, W.M.; Kang, K. Engineering Solid Electrolyte Interphase for Pseudocapacitive Anatase TiO₂ Anodes in Sodium-Ion Batteries. *Adv. Funct. Mater.* **2018**, *28*, 1802099. [[CrossRef](#)]
- Zhao, L.; Yin, J.; Lin, J.; Chen, C.; Chen, L.; Qiu, X.; Alshareef, H.N.; Zhang, W. Highly Stable ZnS Anodes for Sodium-Ion Batteries Enabled by Structure and Electrolyte Engineering. *ACS Nano* **2024**, *18*, 3763–3774. [[CrossRef](#)]

21. Zou, K.; Deng, W.; Silvester, D.S.; Zou, G.; Hou, H.; Banks, C.E.; Li, L.; Hu, J.; Ji, X. Carbonyl Chemistry for Advanced Electrochemical Energy Storage Systems. *ACS Nano* **2024**, *18*, 19950–20000. [CrossRef] [PubMed]
22. Zhang, J.; Li, Q.; Zeng, Y.; Tang, Z.; Sun, D.; Huang, D.; Tang, Y.; Wang, H. Weakly Solvating Cyclic Ether Electrolyte for High-Voltage Lithium Metal Batteries. *ACS Energy Lett.* **2023**, *8*, 1752–1761. [CrossRef]
23. Yin, L.; Wang, M.; Xie, C.; Yang, C.; Han, J.; You, Y. High-Voltage Cyclic Ether-Based Electrolytes for Low-Temperature Sodium-Ion Batteries. *ACS Appl. Mater. Interfaces* **2023**, *15*, 9517–9523. [CrossRef] [PubMed]
24. Yan, D.; Yu, C.; Li, D.; Zhang, X.; Li, J.; Lu, T.; Pan, L. Improved sodium-ion storage performance of TiO₂ nanotubes by Ni²⁺ doping. *J. Mater. Chem. A* **2016**, *4*, 11077–11085. [CrossRef]
25. Feng, W.; Meng, C.; Guo, X.; Wu, B.; Sui, X.; Wang, Z. Defect-Driven Reconstruction of Na-Ion Diffusion Channels Enabling High-Performance Co-Doped TiO₂ Anodes for Na-Ion Hybrid Capacitors. *Adv. Energy Mater.* **2024**, *14*, 2400558. [CrossRef]
26. Yang, X.; Wang, S.; Zhuang, X.; Tomaneč, O.; Zboril, R.; Yu, D.Y.W.; Rogach, A.L. Polypyrrole and Carbon Nanotube Co-Composited Titania Anodes with Enhanced Sodium Storage Performance in Ether-Based Electrolyte. *Adv. Sustain. Syst.* **2019**, *3*, 1800154. [CrossRef]
27. Li, K.; Zhang, J.; Lin, D.; Wang, D.-W.; Li, B.; Lv, W.; Sun, S.; He, Y.-B.; Kang, F.; Yang, Q.-H.; et al. Evolution of the electrochemical interface in sodium ion batteries with ether electrolytes. *Nat. Commun.* **2019**, *10*, 725. [CrossRef]
28. Yang, L.; Yang, Y.; Shi, W.; Leng, S.; Cheng, D.; Hou, H. Ultra-high initial coulombic efficiency of the TiO₂ anode induced by the synergistic role of the electrolyte and binder for sodium-ion batteries. *J. Mater. Chem. A* **2023**, *11*, 17710–17717. [CrossRef]
29. He, Y.; Liu, D.; Jiao, J.; Liu, Y.; He, S.; Zhang, Y.; Cheng, Q.; Fang, Y.; Mo, X.; Pan, H.; et al. Pyridinic N-Dominated Hard Carbon with Accessible Carbonyl Groups Enabling 98% Initial Coulombic Efficiency for Sodium-Ion Batteries. *Adv. Funct. Mater.* **2024**, *34*, 2403144. [CrossRef]
30. Wu, N.; Zhao, Z.; Hua, R.; Wang, X.; Zhang, Y.; Li, J.; Liu, G.; Guo, D.; Sun, G.; Liu, X.; et al. Pre-Doping of Dual-Functional Sodium to Weaken Fe–S Bond and Stabilize Interfacial Chemistry for High-Rate Reversible Sodium Storage. *Adv. Energy Mater.* **2024**, *14*, 2400371. [CrossRef]
31. Wang, Y.; Jiang, N.; Liu, J.; Sun, S.; Wang, X.; Yang, J.; Yang, C.; Liu, Y. Ultralong Lifespan Zero-Cobalt/Nickel Prussian Blue Analogs Cathode Realized by Solid Solution Reaction Sodium Storage Mechanism. *Adv. Funct. Mater.* **2024**, 2406809. [CrossRef]
32. Li, J.; He, Y.; Dai, Y.; Zhang, H.; Zhang, Y.; Gu, S.; Wang, X.; Gao, T.; Zhou, G.; Xu, L. Heterostructure Interface Construction of Cobalt/Molybdenum Selenides toward Ultra-Stable Sodium-Ion Half/Full Batteries. *Adv. Funct. Mater.* **2024**, 2406915. [CrossRef]
33. Tian, S.; Chen, W.; Wang, R.; Qin, C.; Jiang, Z.-J.; Jiang, Z. Ar/NH₃ Radio-Frequency Plasma Etching and N-doping to Stabilize Metallic Phase 1T-MoS₂ for Fast and Durable Sodium-Ion Storage. *Adv. Funct. Mater.* **2024**, 2408035. [CrossRef]
34. Yi, X.; Li, X.; Zhong, J.; Wang, S.; Wang, Z.; Guo, H.; Wang, J.; Yan, G. Unraveling the Mechanism of Different Kinetics Performance between Ether and Carbonate Ester Electrolytes in Hard Carbon Electrode. *Adv. Funct. Mater.* **2022**, *32*, 2209523. [CrossRef]
35. Zheng, Y.-Q.; Sun, M.-Y.; Yu, F.-D.; Deng, L.; Xia, Y.; Jiang, Y.-S.; Que, L.-F.; Zhao, L.; Wang, Z.-B. Utilizing weakly-solvated diglyme-based electrolyte to achieve a 10,000-cycles durable Na₃V₂(PO₄)₂F₃ cathode endured at –20 °C. *Nano Energy* **2022**, *102*, 107693. [CrossRef]
36. Zhang, Y.; Yue, L.; Ding, H.; Xiong, Z.; Bai, L.; Xu, M.; Qi, Y. Carbon dots promoting surface defect and interphase high anion concentration for sodium-ion battery carbon anodes. *Nano Energy* **2024**, *127*, 109696. [CrossRef]
37. Gao, Y.; Wu, G.; Fang, W.; Qin, Z.; Zhang, T.; Yan, J.; Zhong, Y.; Zhang, N.; Chen, G. Transesterification Induced Multifunctional Additives Enable High-Performance Lithium Metal Batteries. *Angew. Chem. Int. Ed.* **2024**, *63*, e202403668. [CrossRef]
38. Liu, M.; Wu, F.; Gong, Y.; Li, Y.; Li, Y.; Feng, X.; Li, Q.; Wu, C.; Bai, Y. Interfacial-Catalysis-Enabled Layered and Inorganic-Rich SEI on Hard Carbon Anodes in Ester Electrolytes for Sodium-Ion Batteries. *Adv. Mater.* **2023**, *35*, 2300002. [CrossRef]
39. Meng, W.; Dang, Z.; Li, D.; Jiang, L. Long-Cycle-Life Sodium-Ion Battery Fabrication via a Unique Chemical Bonding Interface Mechanism. *Adv. Mater.* **2023**, *35*, 2301376. [CrossRef]
40. Cheng, F.; Cao, M.; Li, Q.; Fang, C.; Han, J.; Huang, Y. Electrolyte Salts for Sodium-Ion Batteries: NaPF₆ or NaClO₄? *ACS Nano* **2023**, *17*, 18608–18615. [CrossRef]
41. Wu, L.; Bresser, D.; Buchholz, D.; Giffin, G.A.; Castro, C.R.; Ochel, A.; Passerini, S. Unfolding the Mechanism of Sodium Insertion in Anatase TiO₂ Nanoparticles. *Adv. Energy Mater.* **2015**, *5*, 1401142. [CrossRef]
42. Portenkirchner, E.; Rommel, S.; Szabados, L.; Griesser, C.; Werner, D.; Stock, D.; Kunze-Liebhäuser, J. Sodiation mechanism via reversible surface film formation on metal oxides for sodium-ion batteries. *Nano Sel.* **2021**, *2*, 1533–1543. [CrossRef]
43. Qin, M.; Zeng, Z.; Wu, Q.; Ma, F.; Liu, Q.; Cheng, S.; Xie, J. Microsolvating Competition in Li⁺ Solvation Structure Affording PC-Based Electrolyte with Fast Kinetics for Lithium-Ion Batteries. *Adv. Funct. Mater.* **2024**, *34*, 2406357. [CrossRef]
44. Liu, X.; Zhang, J.; Yun, X.; Li, J.; Yu, H.; Peng, L.; Xi, Z.; Wang, R.; Yang, L.; Xie, W.; et al. Anchored Weakly-Solvated Electrolytes for High-Voltage and Low-Temperature Lithium-ion Batteries. *Angew. Chem. Int. Ed.* **2024**, *63*, e202406596. [CrossRef] [PubMed]

Disclaimer/Publisher's Note: The statements, opinions and data contained in all publications are solely those of the individual author(s) and contributor(s) and not of MDPI and/or the editor(s). MDPI and/or the editor(s) disclaim responsibility for any injury to people or property resulting from any ideas, methods, instructions or products referred to in the content.